THREE-DIMENSIONAL BLUFF BODY AERODYNAMICS AND ITS IMPORTANCE FOR HELICOPTER SLING LOADS

Daniel T. Prosser Marilyn J. Smith
School of Aerospace Engineering
Georgia Institute of Technology
Atlanta, Georgia, 30332-0150, USA

ABSTRACT

Fundamental three-dimensional aerodynamic phenomena have been investigated for small-aspect-ratio rectangular prisms and circular cylinders, canonical bluff body geometries representative of typical helicopter sling loads. A detailed identification and quantification of the unsteady aerodynamic phenomena at differing orientation angles associated with instabilities has been undertaken. The numerical experiments indicate that shear layer reattachment is the primary factor in determining the mean forces and moments of the bluff bodies. Many characteristics of the shear layer behavior are similar for the three-dimensional bluff bodies and, in some cases, similar to two-dimensional behavior extant in the literature. Differences in the canonical shape and aspect ratios occur and are quantified with varying reattachment distances as the orientation changes. Strouhal numbers vary in the range from 0.15–0.3 and exhibited a highly three-dimensional, multimodal nature at the Reynolds numbers investigated. These findings are significant for the development of reduced-order aerodynamic modeling of sling loads.

NOTATION

c_p	Pressure coefficient, $c_p = \frac{2(p-p_\infty)}{\rho_\infty U_\infty^2}$
D	Diameter, m
H	Height, m
L	Length, m
L_{ref}	Reference length, m
p_∞	Reference pressure, Pa
S_{ref}	Reference area, m^2
St	Strouhal number, $St = \frac{fL_{ref}}{U_\infty}$
t	Time variable, sec
$\boldsymbol{U}_\infty$	Reference velocity vector, m/sec
W	Width, m
x	Separation bubble width, m
α, β	Angles of attack and yaw, deg.
ρ_∞	Reference density, kg/m^3

1 INTRODUCTION

Hurricanes, earthquakes, wildfires, search and rescue – these words evoke events in recent times in which rotary wing vehicles have played a major role on the global stage. The helicopter's ability to access and hover over locations no other vehicle can efficiently reach is a key aspect in delivery or retrieval of emergency hospitals, shelters, and people, as well as potable water and supplies. These missions are accomplished by tethering the load beneath the helicopter, giving rise to the term *slung load* or *sling load* operations. Unfortunately, the addition of these tethered loads requires that each differing load configuration be separately flight tested for safety, as they can become unstable at higher flight speeds within the envelope [1–3]. For example, while the power-limited forward speed of the UH-60 helicopter with the CONEX cargo container is above 100 knots, the stability-limited forward speed is 60 knots[3]. This restriction results in slower rescues and fewer deliveries in emergency situations. Significant costs can be saved if the requirement to test each payload can be reduced[4].

To achieve this goal of reducing flight tests, it is first necessary to understand the aerodynamic-dynamic interaction of these bluff bodies so that the mechanisms that drive instabilities can be characterized and quantified. While a significant body of research exists in the literature on the aerodynamics of two-dimensional bluff bodies such as long circular cylinders and rectangular prisms, in comparison much less information is available for three-dimensional bluff bodies. Two-dimensional (2-D) aerodynamics is sufficient for bluff bodies with one geometric dimension much larger than the other two, and their applications include design and analysis of bridges, power lines, oil platforms, and towers [5–9]. Tethered loads, such as those associated with sling loads or air drops,

Presented at the 40th European Rotorcraft Forum, Southampton, UK, September 2–5, 2014.

typically do not fall in the category of 2-D bodies; all geometric dimensions are on the same order of magnitude, and 3-D aerodynamic interactions are very important. Furthermore, a wide range of incidence angles and flow conditions may be encountered, requiring an understanding of the physics for more than one or two discrete orientations.

In the past decade, a number of evaluations of dynamic instabilities in wind tunnel testing, flight testing, computations fluid dynamics (CFD) simulations, and reduced-order modeling have been undertaken with different goals. Raz et al. [10] and Cicolani et al. [11] have focused on passive stabilization of tethered load dynamics by applying aerodynamic fins to the tethered load. Raz et al. [12] have also investigated coupled helicopter-load dynamics and pilot-induced oscillations in tethered load operations via flight tests. Prosser and Smith[13] have demonstrated that current three-dimensional unsteady Reynolds-averaged Navier Stokes (URANS) computations with large-eddy-simulation (LES) turbulence closure in the wake, coupled with a 6-DoF rigid body motion solver, can accurately simulate the dynamics of a tethered load.

While these approaches have advanced the state of the art in understanding the instabilities of the tethered loads, they all require significant costs in either physical or numerical unsteady testing. To alleviate these high costs and time requirements, researchers are seeking to develop empirical models based on unsteady physics. Some of the foundational work in this area includes Greenwell[2], Cicolani and da Silva[14], and Cone [15]. Prosser and Smith [16,17] have developed empirical correlations for bluff body aerodynamics. These approaches and findings are particularly important as they are based in physics rather than curve-fits for specific configurations resulting in mathematical "black boxes," so that the physics-based models hold the promise of expansion to a wide range of load configurations and applications.

Fundamental research at the Georgia Institute of Technology (GT) seeks to understand the interactional physics of these dynamic bluff bodies and advance the knowledge associated with 3-D dynamic configurations. From these fundamental findings, efficient, accurate, physics-based simulation tools to model these interactions can be developed. These simulation tools will permit pilot training, as well as the development of control laws, handling qualities, and stabilization devices. In the longer term, with careful certification from flight tests, these simulation tools hold the promise of reducing flight testing and the development of techniques to permit expansion of the flight envelope to directly impact the rescue and humanitarian role of rotorcraft.

High-fidelity numerical experiments resolve the flow at different orientations for two canonical 3-D bluff body types found in tethered loads: rectangular prisms and cylinders. The computational experiments include error assessment and are validated against experimental data, where available. This numerical approach has a number of advantages over experimental methods, most importantly that extremely rich and detailed information about the flow field can be readily extracted. As a result, aerodynamic phenomena responsible for significant changes in the loading over a range of orientations and Reynolds numbers can be identified and quantified.

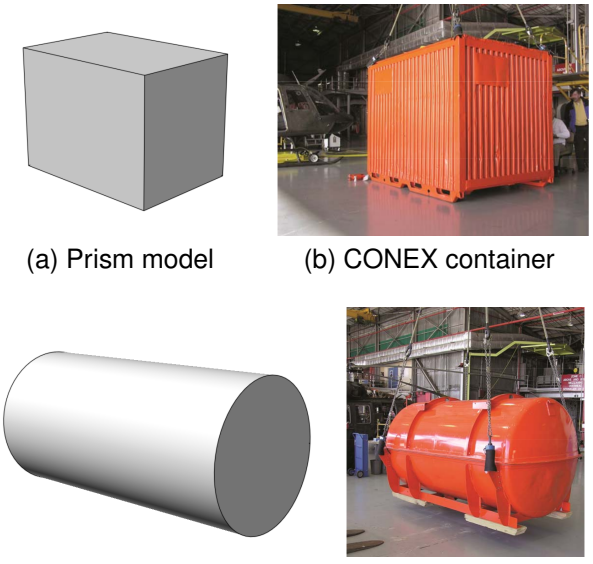

(a) Prism model (b) CONEX container

(c) $L/D = 2$ cylinder (d) Enginer canister

Fig. 1: Bluff body types modeled and the full-scale sling loads they represent[19].

2 CONFIGURATIONS

Two bluff bodies were selected for this study: the rectangular prism (Fig. 1(a)) and the circular cylinder (Fig. 1(c)). The rectangular prism is a smooth representation of the 6 ft. x 6 ft. x 8 ft. Container Express (CONEX) cargo container Fig. 1(b)). Prior evaluations[10,18] have indicated that the corrugations do not play a major role in the aerodynamic instabilities. Short finite cylinders with two different aspect ratios, $L/D = 1$ and $L/D = 2$, were also selected. The cylinders are also representaive of common tethered loads; for instance, engine canisters and oil drums (Fig. 1(d)). Both types of loads may be considered *canonical* geometries, meaning that they are basic configurations that may be used to study fundamental aerodynamic behaviors which also apply to more complex configurations. These canonical geometries are also pervasive in many applications outside the tethered loads problem, so the conclusions drawn herein are broadly pertinent.

The dimensions and flow conditions for the vari-

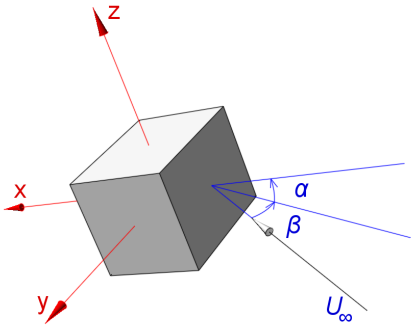

Fig. 2: Convention for the orientation angles α and β.

ous bluff bodies are presented in Tables 1 and 2. In some cases, the flow conditions applied are dictated by the availability of anticipated experimental data. To ensure that valid conclusions regarding the effects of aspect ratio for the cylinder can be made, case 3 has been added to the present numerical study. It is expected that the rectangular prism should be fairly insensitive to Reynolds number as leading-edge separation is triggered by its sharp edges, as noted by other investigators [10,12]. Conversely, the cylinder may be more sensitive to the Reynolds number when separation occurs on its smooth curvilinear surface.

Table 1: Prism dimensions and flow conditions

L	W	H	Re	α	β
0.232	0.165	0.176	2.12×10^5	0	0 – 90

Table 2: Cylinder dimensions and flow conditions

No.	L	D	Re_D	α	β
1	0.2191	0.2191	0.96×10^5	0	0 – 90
2	0.4382	0.2191	1.56×10^5	0	0 – 90
3	0.4382	0.2191	0.96×10^5	0	0 – 90

In each case, the angle of attack is held at 0 degrees while the yaw angle is changed from 0 to 90 degrees. The convention used to define the angle of attack and the yaw angle is illustrated in Fig. 2. For both geometries, $\beta = 0$ corresponds to the orientation in which the length dimension is perpendicular to the free-stream velocity.

3 NUMERICAL EXPERIMENTS

The approach for the numerical experiments has been leveraged from prior algorithm development by Lynch [20], Shenoy [21], and Prosser [13]. The numerical experiments employ the well-validated NASA solver, FUN3D [22], which is capable of solving the incompressible or compressible Reynolds-averaged Navier-Stokes (RANS) equations on mixed-element unstructured grids in steady-state or time-accurate (unsteady) flows. To extend the unsteady RANS (or URANS) turbulence approach to flows with large regions of separation, a hybrid turbulence approach has been developed in the last decade and implemented into the FUN3D code [20,20,23]. The hybrid approach couples URANS in the near-wall regions with large-eddy simulation (LES) in the wake, permitting large eddies in the separated wake to be resolved without requiring an excessively fine grid. This hybrid turbulence approach has been validated for unsteady bluff body configurations [20,24,25].

FUN3D also incorporates overset grid capability via the SUGGAR++ and DiRTlib libraries [26,27]. A near-body grid is placed on top of a background grid, and flow field information is interpolated between the two grids at the boundaries of the near-body grid. This approach allows the same grids to be re-used in multiple orientations, while also simplifying the grid generation process for complex geometries. Overset grid adaptation [21] permits fine resolution of flow details at each yaw angle.

In this work, the flow conditions correspond to very low Mach numbers (below 0.1), so the incompressible path in FUN3D is utilized. The incompressible path in FUN3D is implemented through Chorin's method of artificial compressibility [28]. The spatial formulation is an implicit node-centered finite-volume scheme, with inviscid fluxes computed using Roe's flux-splitting method and viscous fluxes evaluated using least-squares gradients equivalent to a second-order central difference scheme. Though the configurations are static, the flow is highly unsteady and thus a time-accurate solution is required. To this end, a second-order backward differention temporal integration scheme is applied.

3.1 Grid Studies

Grids were created for the bluff body geometries using best practices established for similar configurations with the hybrid URANS/LES approach [20,24,25]. The boundary layer region of the grids used prismatic elements aligned with the wall-normal direction; at least 35 cells in the normal direction with a non-dimensional wall spacing (y^+) of less than 1.0. This boundary layer spacing is necessary to correctly capture separation and reattachment on surfaces at high angles normal to the flow [20,24,29].

External to the boundary layer, the mesh topology was tetrahedral. Prior grid studies [13,20,24,25] were used to establish grids that result in integrated forces, pressures, and separation locations with correlated experimental error limits (where available). As the data are or will later be correlated with wind tunnel data, the near-body grids are superimposed on background meshes to simulate wind tunnel test sections;

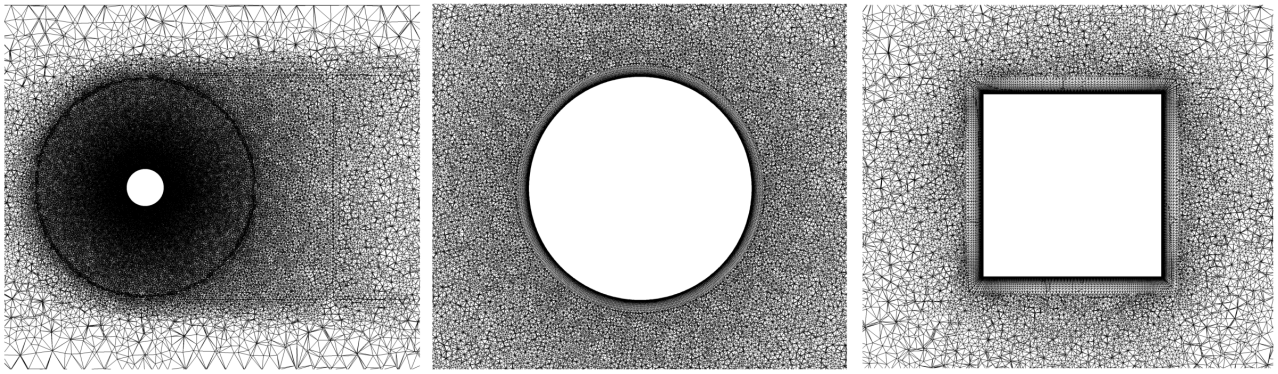

(a) Cylinder and wind tunnel grids (b) Cylinder near-body grid (c) Prism near-body grid

Fig. 3: Side-views of bluff body overset grids.

the tunnel walls extended 10.5 diameters upstream and downstream of the model. While initial numerical studies have indicated that wall blockage is minimal, for consistency all comparisons are made with the same wind tunnel test section. The model mounting apparatus is not included to avoid interactions not present for true canonical geometries.

Three side-views of the grids are presented in Fig. 3. Figure 3(a) illustrates the $L/D = 1$ cylinder grid from a perspective that includes the top and bottom walls of the wind tunnel. Figure 3(b) presents the same view, but from a closer perspective so that the boundary-layer region is visible. Special care was taken in the development of the cylinder configuration as the separation point along the curvilinear surface varies with Reynolds number. The grid structure and mesh count applied in these studies predict separation and surface pressure distributions within the experimental errors at a Reynolds number of 3500[20] and have been confirmed for Reynolds numbers comparable to that of this study [25] using the same URANS/LES turbulence closure. The cylinder overset grids required 6.0 million nodes.

Figure 3(c) depicts the rectangular prism grid, which is less refined than the cylinder grid. The presence of the edges along each side of the box results in fixed separation points, so that the detailed refinements along the flat sides necessary for the cylinder were not required. The prism overset grid contains 3.5 million nodes. This configuration was demonstrated in a prior study to result in prediction of the time-averaged aerodynamic forces and moments within experimental error bounds[13], and further validation is presented in Section 4.

3.2 Error Determination

Shenoy [30] demonstrated that the spatial and temporal errors for overset unstructured meshes for complex bluff bodies applying the URANS/LES turbulence closure with and without adaptive grids can be assessed and quantified. The results of his error analysis have been applied in this study, guaranteeing second order spatial and temporal accuracy.

Because of the unsteady shedding of the static bluff bodies, an additional error analysis has been undertaken. Similar to the wind tunnel and computational studies in the 1980s for dynamic stall (e.g. [31],) the static predictions of the $L/D = 1$ cylinder have been compared to a slowly rotating cylinder at 1 RPM. This comparison provides an estimate of the errors due to differing yaw angles (i.e. measurement errors in wind tunnel and flight tests) as well as an indication of how the fluctuation behavior may change in steady and quasi-steady flows. Figure 4 presents the relevant integrated forces and moments for this comparison. The static simulations include minimum and maximum bounds to give an indication of the unsteadiness. With very few exceptions, the rotating case results fall within these bounds. However, the rotating case does provide a more detailed picture of where changes in trends occur; e.g., the slope changes in drag and side force coefficients between $\beta = 75^\circ$ and 80°.

Finally, where there are experimental data available, the numerical experimental results have been compared. These comparisons are primarily integrated force and moment data and are included in the figures and discussions in the following section.

4 RESULTS AND DISCUSSION

4.1 Force and Moment Coefficients

Static force and moment coefficients have been compiled for the rectangular prism and circular cylinders with β ranging from 0 to 90 degrees. These are compared with wind tunnel experiments performed at the Georgia Institute of Technology [32] and external data,

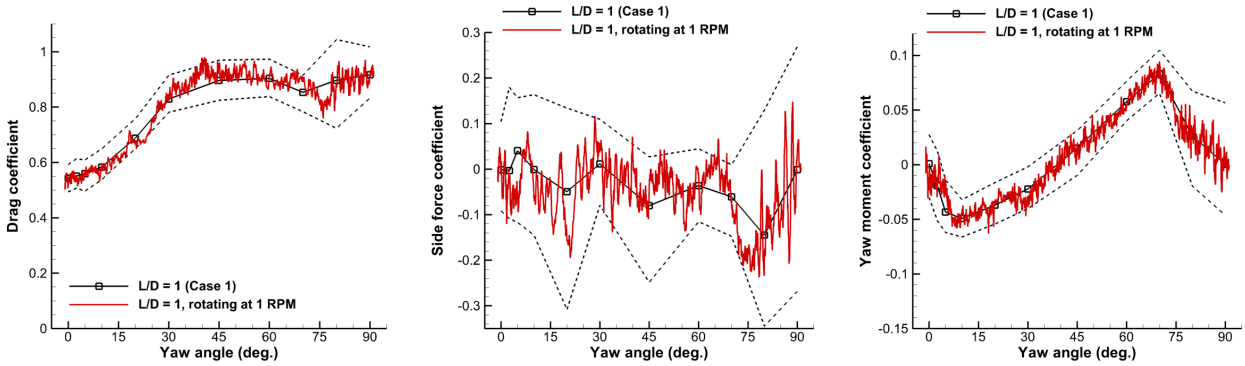

(a) Drag coefficient (b) Side force coefficient (c) Yaw moment coefficient

Fig. 4: Static and rotating (1 RPM) $L/D = 1$ cylinder static integrated aerodynamics.

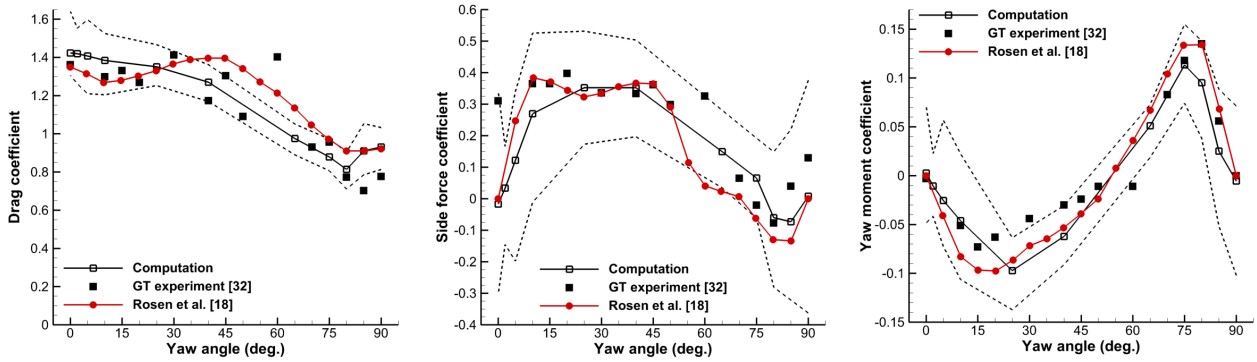

(a) Drag coefficient (b) Side force coefficient (c) Yaw moment coefficient

Fig. 5: Rectangular prism computed force and moment coefficients and comparison with experimental data[18,32]. The average face area is used as the reference.

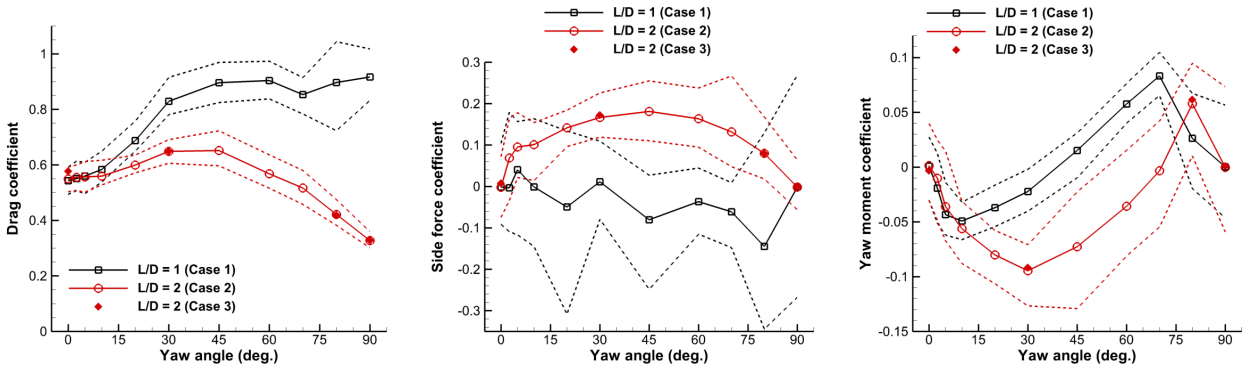

(a) Drag coefficient (b) Side force coefficient (c) Yaw moment coefficient

Fig. 6: Circular cylinder computed force and moment coefficients. The planform area LD is used as the reference.

where available. The external data are by Rosen et al. [18], which used a smaller-scale model of the same CONEX container. The Reynolds number in that case, based on the average of length and width, was 1.8×10^5, which is lower than but still comparable to the current numerical experiments. The bounding curves, denoted by dotted lines, for both the prism and cylinder computations are not uncertainties, but rather an indication of the magnitude of unsteady fluctuations. These are constructed using the minimum and maximum values of the coefficients in each orientation.

Figures 5 and 6 depict the static force and moment coefficients for the prism and cylinder computations. The drag force is defined as the force parallel to the flow direction, and the side force is perpendicular to this direction in the horizontal plane, and the yaw moment is about the vertical axis. The time-averaged forces and moments are demarked by open symbols and connected with a line, while the fluctuations are represented as dotted lines.

The agreement between the prism force and moment coefficients with both sets of experimental data is quite good. There is some variation between the two sets of wind tunnel test data, but in general at least one of the two experimental data sets lies within the bounds of unsteadiness of the computations. The greatest disparities between all three sets of data occur in the drag coefficient, but the computed drag is generally in between the two experimental values in the regions where disparities occur. Overall, the computational predictions presented here are the best available in the literature to date. This good agreement is attributed in large part to the hybrid turbulence approach which permits the resolution of large turbulent structures in the wake. Prior efforts with traditional RANS turbulence models have been less successful, particularly in the prediction of side force[11].

The force and moment curves for the rectangular prism are characterized by significant nonlinearities. At low yaw angle, the side force and yaw moment coefficient trends are linear. In these conditions, the forces and moments are dominated by the difference between stagnation pressure and base pressure on the front and back sides, which rotates with the prism. An abrupt change in both the side force and yaw moment coefficients occurs between $\beta = 10^\circ$ and $\beta = 30^\circ$, arresting the linear trend. This behavior has been studied in detail by Greenwell [2] for 2-D rectangular prisms. A shear layer phenomena known as *reattachment* on the sides of the prism is responsible for the behavior, which will be investigated in detail in the following sections. Over a range of yaw angles, the side force coefficient remains approximately constant. Prosser and Smith [16] demonstrated that this range can be predicted as a function of the ratio L/W for a wide range of 2-D and 3-D rectangular prisms.

Figure 6 presents the drag, side force, and yaw moment for the circular cylinders identified in Table 2. The drag coefficient for the two different aspect ratios initially is equal at $\beta = 0$ and subsequently begins to increase. For $L/D = 1$, the drag coefficient reaches a nearly constant maximum value beginning at $\beta = 45^\circ$, but for $L/D = 2$ it reaches a peak and then decreases again. The force coefficients here are normalized by LD, which is different for the two different aspect ratios, so at $\beta = 90^\circ$ the disparity in dimensional drag is not as large as the drag coefficient difference. However, the dimensional drag is nonetheless smaller for the $L/D = 2$ case than for $L/D = 1$ by 30% at $\beta = 90^\circ$. This result is supported by data presented by Hoerner [33], which indicates that the drag increases for cylinders in axial flow as the aspect ratio decreases below two. Hoerner's data also indicate that, for cylinders in crossflow ($\beta = 0$), the drag coefficient remains approximately constant for aspect ratios below five, which confirms the present result.

Comparing the magnitude of the drag coefficients with experimental data from the literature, it is apparent that the cylinders are in transitioning flow when separation occurs from the curvilinear surface at $\beta = 0$, but in supercritical flow when separation occurs from the sharp edges at $\beta = 90^\circ$. The drag coefficient for both cylinders at $\beta = 0$ is 0.55, which is between the subcritical experiments ($C_D = 0.7$) and supercritical ($C_D = 0.3$) [34]. At $\beta = 90^\circ$, the drag coefficient for $L/D = 1$ is 1.16 (when normalized by $\pi D^2/4$ instead of LD), which is equal to experimental data from Hoerner [33] for supercritical flow. The drag coefficient for the $L/D = 2$ case is 0.83 at $\beta = 90^\circ$, which is also consistent with the Hoerner data. The mixed flow conditions in these numerical experiments should be considered when applying to full-scale problems.

The side force coefficient is distinctly different for the two different aspect ratios. The side force for $L/D = 1$ is characterized by very large fluctuations and an overall erratic trend with β. In contrast, for $L/D = 2$ the fluctuations are relatively much smaller and the trends are similar to the rectangular prism, albeit without the negative values near $\beta = 90^\circ$. The yaw moment coefficient behavior is very similar for the two cylinders, though the abrupt changes occur at different yaw angles, and the behavior is also remarkably similar to the yaw moment coefficient for the prism. Only small differences exist between the force and moment coefficients for the two $L/D = 2$ cylinders at different Reynolds numbers (cases 2 and 3), so subsequent analyses utilize the data from case 2 despite the slightly higher Reynolds number relative to case 1.

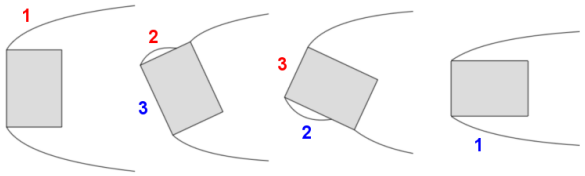

Fig. 7: Illustration of shear layer separation and reattachment behavior for a rectangular prism. (1) Fully separated shear layer, (2) reattaching shear layer, and (3) fully attached flow.

4.2 Shear Layer Behavior

The sudden changes in the force and moment coefficients for both the rectangular prism and the cylinder are caused by changing shear layer behavior. Consider Fig. 7, which illustrates three distinct shear layer behaviors for the rectangular prism. At low yaw angles, the right short side, labeled in red, is in completely separated flow, while the flow is fully attached on the front long side. As the yaw angle increases, the flow remains attached on the long side, and a separation bubble forms on the short side. Further increasing the yaw angle causes the flow to be fully attached on the short side, but a separation bubble grows on the long side. Finally, the shear layer separates completely on the long side.

Similar behaviors are also present for the cylinder. At low to mid yaw angles, reattachment occurs on the flat face of the cylinder. Eventually, attached flow is experienced on the flat face, and in turn a separation bubble begins to form on the curvilinear face. The particular angles and characteristics of shear layer behavior for the two types of bluff bodies are investigated in detail later in the following sections.

4.3 Unsteady Flow Characteristics

Despite the static configurations, the flow fields around 3-D bluff bodies are highly unsteady. At sufficiently high Reynolds numbers, as in sling load applications, the wake is highly turbulent, producing complex eddies. Figure 8 illustrates this complex flow behavior for the rectangular prism at yaw angles of 10 and 25 degrees. In this figure, the freestream flow impinges on the prism from right to left. Snapshots of the flow are rendered via iso-surfaces of $Q = 500$ in light gray, while the surface of the prism is colored by the pressure coefficient. Q is defined as $Q = \frac{1}{2}\left(||\Omega||^2 - ||S||^2\right)$, where Ω is the vorticity and S is the rate of strain. In Fig. 8, all velocities are non-dimensionalized by the freestream flow speed, while lengths are non-dimensionalized by 1 meter, also making Q a non-dimensional quantity. Vorticity dominates in regions where Q is positive, which occurs in turbulent eddies and other coherent structures, while strain rate dominates in regions where it is negative, in boundary layers, for instance.

Figure 8 reveals that the flow behavior on the right side of the prism is markedly different between $\beta = 10^\circ$ and $\beta = 25^\circ$. At $\beta = 10^\circ$, the shear layer on this side breaks up into eddies, and these subsequently interact with those above and below the prism as they are convected downstream. In contrast, at $\beta = 25^\circ$, the shear layer begins to break apart but then impinges on the surface on the bluff body and disappears because it is reincorporated into the boundary layer. This is the reattachment phenomenon which causes significant changes in the mean forces and moments. The pressure signature on the right side is markedly different between $\beta = 10^\circ$ and $\beta = 25^\circ$ and is responsible for these changes in integrated quantities. As soon as the shear layer reattaches, the pressure coefficient suddenly increases drastically, creating a force in the negative y-direction and a positive contribution to the pitching moment as the attachment location moves forward.

Figure 8(c) presents a top-down sliced view of the flow field for the $L/D = 1$ cylinder (case 1 from Table 2) at $\beta = 2.5^\circ$. In this figure, the flow field is colored by Q, indicating the locations of vortices and interaction between vortices and the boundary layer. In the case of the cylinder, some reattachment occurs on the right side at this low yaw angle. As in the case of the prism, the shear layer is initially formed by forced separation at the edge, and it eventually begins to break apart as it moves downstream. Between the shear layer and the right face of the cylinder, there is a separation bubble region where large coherent structures are not present. Further downstream, the shear layer, having now broken apart into large vortices, begins to interact with the surface and then weakly reattach near the back of the right flat face. The behavior of the shear layer is similar on the left side, but no significant reattachment occurs.

4.4 Time-Averaged Behavior

It has been demonstrated that the behavior of the flow around 3-D bluff bodies is highly unsteady and turbulent, and that reattachment of the shear layer plays an important role in determining the forces and moments. The significant unsteadiness makes it difficult to characterize the flow phenomena that drive the *mean*, or time-averaged, forces and moments. Therefore, it is beneficial to time-average the flow fields themselves so that the mean separation and reattachment behavior may be studied.

To illustrate the effect over time, Fig. 9(a) presents the time-averaged unsteady flow field of Fig. 8(c). The scale for Q has been reduced as the time-averaging process smears the vortices, reducing the

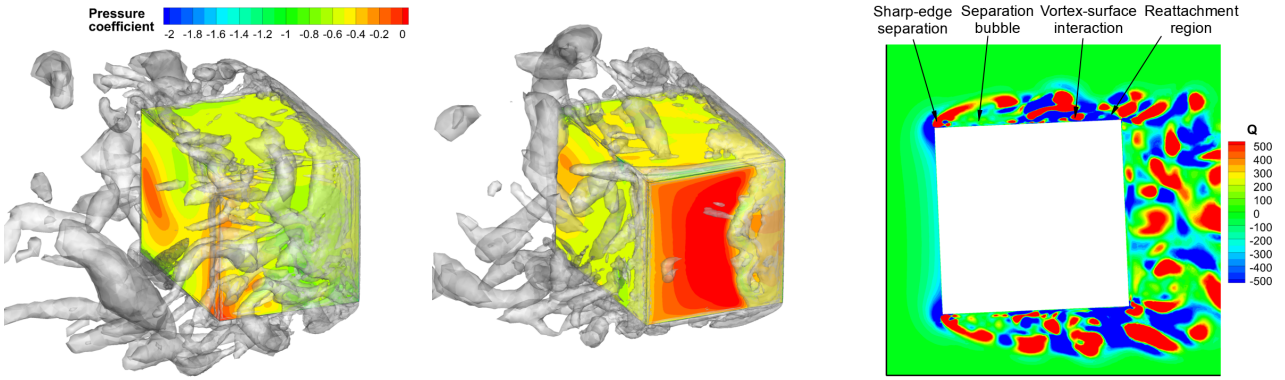

(a) $\beta = 10^\circ$ (b) $\beta = 25^\circ$ (c) $L/D = 1$ cylinder, $\beta = 2.5^\circ$

Fig. 8: Instantaneous flow fields. For the prism, Q iso-surfaces are shown in gray and the flow is from the right; for the cylinder, the flow field is colored by Q and the flow is from the left.

maximum vorticity. Though the time-averaging filters out discrete structures, it is now possible to visualize the location of separation and reattachment of the shear layer from the surface. At $\beta = 2.5^\circ$, some reattachment occurs near the back of the right side. As the yaw angle increases (Fig. 9(b) and (c)), the reattachment becomes stronger and the location moves forward. On the left side of the cylinder, shear layer-surface interactions become weaker as the shear layer separates further from the surface.

Reattachment pressure distributions for both cylinders (cases 1 and 2) and the rectangular prism are presented in Fig. 10. For the cylinder, reattachment occurs either on one of the flat faces for yaw angles below $\beta = 45^\circ$or on the curvilinear face for angles above $\beta = 45^\circ$. Reattachment pressures for these two different faces are given in separate plots, Figs. 10(a) and (b). The reattachment pressure distributions for the rectangular prism are depicted in Fig. 10(c). In each of these figures, the abscissa is normalized by a reference length. In the case of the cylinders, the reference length is the diameter, and in the case of the rectangular prism, it is the length of the side on which reattachment occurs. The pressure distributions shown are taken in a slice along the centerline of the bluff body.

Several similarities are apparent among all three sets of reattachment pressure distributions. The distributions are made up of two distinct components; a separated flow component of relatively low pressure within the separation bubble region, and an attached flow component of higher pressure after reattachment takes place. These two components are joined by a transitional region, and reattachment is considered complete when the pressure distribution reaches a positive peak, c_{pmax}. The pressure within the separation bubble region is nearly constant or slightly decreasing, with a minimum pressure of c_{pmin}. The pressure within the separation bubble and the attached-flow region exhibit a similar dependence on the yaw angle. When the yaw angle is such that reattachment just begins to occur (and the bubble is large), the magnitudes of the pressure in both regions is not very sensitive to yaw angle. However, once the attached-flow region begins to be dominant, the pressures in both regions increase quickly with further reductions in separation bubble width. This behavior is common to both the cylinder and rectangular prism and also consistent with data for 2-D rectangles from the literature[35].

The width of the separation bubble region itself is strongly dependent on the yaw angle, with the width of the bubble decreasing as the side where reattachment occurs is turned into the flow. This behavior is apparent in Fig. 9 for the cylinder at low yaw angles, and Fig. 10 demonstrates that the same behavior persists for both geometries over a broad range of yaw angles. Here, the width of the separation bubble is denoted by x in Fig. 10(a). Greenwell[2] demonstrated that, for 2-D rectangular bluff bodies, the variation of reattachment distance with angle of incidence of the face collapses onto a single curve when L_{ref} is taken as the length of the side normal to the side with reattachment. These data are presented in Fig. 11. The curve fit for the 2-D rectangle data was originally developed by Greenwell, while the raw rectangle data originate from a number of sources in the literature[7,35–38].

Figure 11 suggests that the non-dimensional attachment point for the 3-D rectangular prism analyzed here falls onto the same universal curve developed by Greenwell for 2-D rectangles. This is a significant result, because it implies that the 2-D relation can be used to predict the reattachment behavior for 3-D rectangles as well. However, the 3-D rectangular prism studied here represents only a single case,

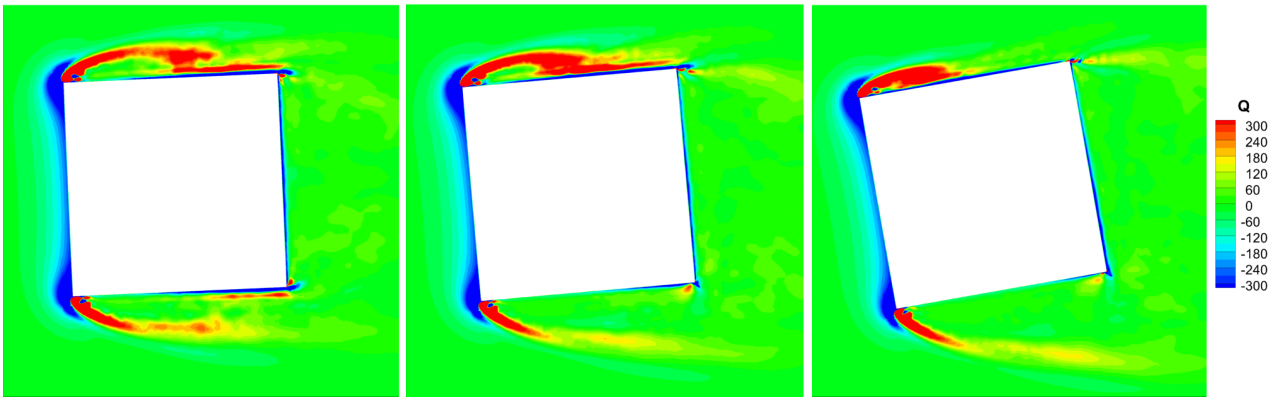

(a) $\beta = 2.5^\circ$ (b) $\beta = 5^\circ$ (c) $\beta = 10^\circ$

Fig. 9: Time-averaged reattachment behavior for the $L/D = 1$ cylinder in a top-down slice of the flow field. The flow field is colored by Q, and the flow is from the left.

and Greenwell[2] noted that the data for a different 3-D rectangular prism fall below the 2-D trend line.

Data for the cylinders are also included in this figure, separated into two sets representing reattachment on the flat face or the curvilinear face. The reference length for the cylinder is taken as the diameter, D. Compared to the rectangular prism, x/L_{ref} is smaller for the cylinder than for the rectangular prism. The reattachment distance varies with the type of reattachment (flat or curvilinear face), but not significantly with L/D. The two different reattachment trends for the cylinder begin to converge as the incidence angle exceeds 20° and the separation bubble width, x, is less than $D/2$.

4.4.1 Influence on Forces and Moments

Figures 5 and 6 indicate that shear layer reattachment has a significant effect on the forces and moments of both the rectangular prism and the circular cylinder. However, it is difficult to determine exactly the influence of reattachment from these figures, because the overall forces and moments include the net effect of all sides combined. Therefore, it is instructive to instead compute the forces and moments on individual faces where reattachment is known to occur. Figure 12 presents the normal force and yaw moment coefficients for the individual faces with reattachment for the rectangular prism. The force coefficients are normalized by the face area, while the moment coefficients are normalized by the face area and side length, and moments are taken about the center of the face. The three different regions denoted in Fig. 7 are marked: (1) fully separated shear layer, (2) reattaching shear layer, and (3) fully attached flow. The long and short sides are color-coded according to the convention from Fig. 7.

Figure 12(a) demonstrates that the changing shear layer behavior is immediately related to changes in the normal force acting on the individual face of the prism. The separated flow region (1) is characterized by a constant negative normal force arising from the low pressure in the separated region. When shear layer reattachment occurs (2), a positive linear trend begins. This change occurs because of the relatively higher pressure in the attached flow region, and the normal force continues to increase as the separation bubble shrinks and the attached flow region grows. In the fully attached flow region (3), the normal force continues to rise and finally reach a maximum when the stagnation point reaches the center of the face. These trends do not significantly change with side length; the only difference is the angle at which reattachment occurs as ascertained in Fig. 11.

The influence of shear layer behavior is also readily apparent in the yaw moment (Figure 12(b)) though the changes are larger than in the normal force, and there are also greater differences depending on the side length. In the separated flow region (1), the yaw moment magnitude slowly changes as the yaw angle is increased. When reattachment occurs (2), the yaw moment trend does not immediately reverse like the normal force trend. Instead, it initially becomes more severe because of the higher pressure on the aft portion of the face and the lower pressure on the forward portion. As the bubble shrinks, the high pressure region begins to cover the forward portion as well, and the yaw moment about the face center abruptly changes sign. It returns towards zero in the fully attached flow region (3). The fact that the yaw moment does not immediately reverse sign in the reattaching region is also reflected in the overall yaw moment for the prism in Fig. 5(c). In contrast, the side force trend immediately responds to reattachment, as is apparent in Fig. 5(b).

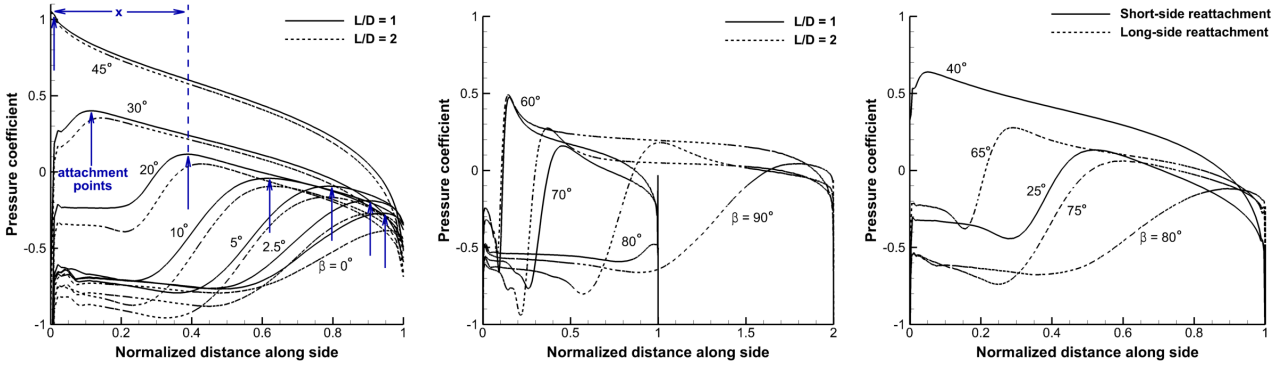

(a) Cylinders: flat face (b) Cylinders: curvilinear face (c) Rectangular prism

Fig. 10: Reattachment pressures for (a) cylinders with reattachment on the flat face, (b) cylinders with reattachment on the curvilinear face, and (c) rectangular prisms.

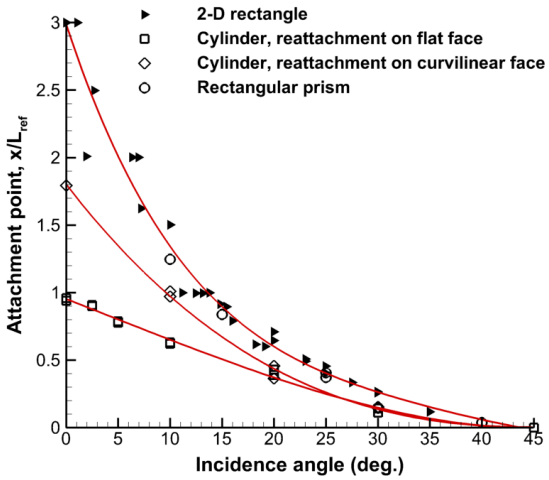

Fig. 11: Non-dimensional attachment distance, x/L_{ref}, for curvilinear and rectangular geometries.

Figure 13 depicts the normal force and yaw moment acting on the flat face of the cylinders. The forces and moments are normalized by the area of the face, $\pi D^2/4$, and the diameter of the cylinder, and yaw moments are taken about the center of the face. Reattachment occurs on the flat face even at $\beta = 0$ for both cylinders, so behavior 1 (completely separated flow) from Fig. 7 is absent. Reattaching and fully attached shear layer behaviors still occur, and their characteristics are very similar to that of the rectangular prism. Notably, the behaviors are nearly identical for $L/D = 1$ and $L/D = 2$ cylinders; the shear layer behavior and its influence on the forces and moments for the flat faces are independent of the aspect ratio for these cases.

The forces and moments have also been computed on the individual curvilinear faces for both cylinders. To isolate the influence of reattachment, these are only summed over the half of the curvilinear face on which reattachment occurs. The area reference for normalizing forces and moments is the projected curvilinear face area, LD, and the reference length is L. Yaw moments have been computed about the centroid of the half-curvilinear face (Fig. 14).

Unlike on the flat faces of the cylinder, the shear layer behavior does depend on the aspect ratio here. The main reason for this difference is that, for $L/D = 2$, the fully-separated shear layer regime (1) is completely absent, while it is present for $L/D = 1$. This difference can be predicted from Fig. 11, which indicates that reattachment on the curvilinear face occurs at $x = 1.8D$ when the incidence angle is $0°$. Reattachment at $x = 1D$ does not occur for curvilinear faces until the incidence angle is $10°$. Thus, fully-separated shear layer behavior (1) persists for the $L/D = 1$ cylinder from $\beta = 90°$ to $80°$, but it never occurs for the $L/D = 2$ cylinder. The influence of the three shear layer behaviors on the forces and moments is similar among all three geometry types. The same trends and characteristics are present on both cylinder faces (flat or curvilinear) and on the prism.

4.5 Strouhal Numbers

Strouhal numbers were determined by sampling the velocity signal in the wake downstream of the bluff bodies. The “virtual hotwire” was placed four diameters downstream for the cylinders and four times the average of L and W downstream for the rectangular prism. A fast Fourier transform (FFT) was used to convert the signal to the frequency domain, and the dominant frequency was taken as the shedding frequency. The results are plotted in Fig. 15.

The Strouhal numbers exhibit no consistent trend with yaw angle variation. Due to the highly aperiodic nature of the turbulent 3-D flow, the frequency content of the signals sometimes contained multiple peaks of similar magnitude, making it difficult to assign a single

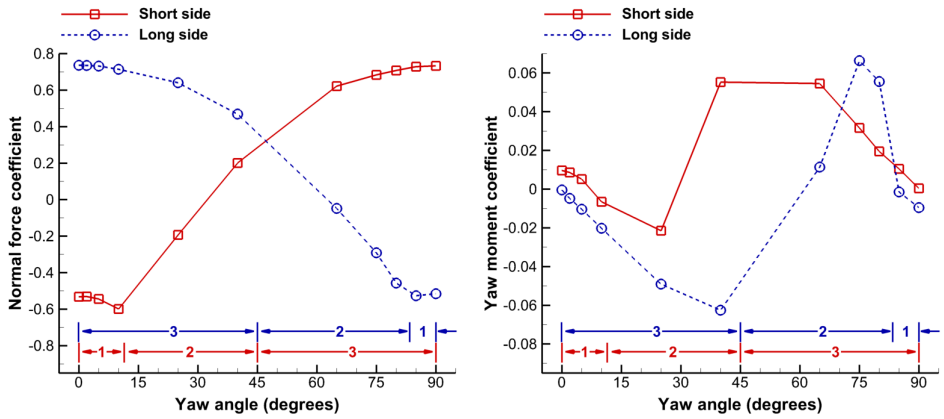

(a) Normal force coefficient (b) Yaw moment coefficient

Fig. 12: Normal force and yaw moment coefficients on individual faces with shear layer reattachment for the rectangular prism. The extents of the three shear layer behaviors from Fig. 7 are labeled.

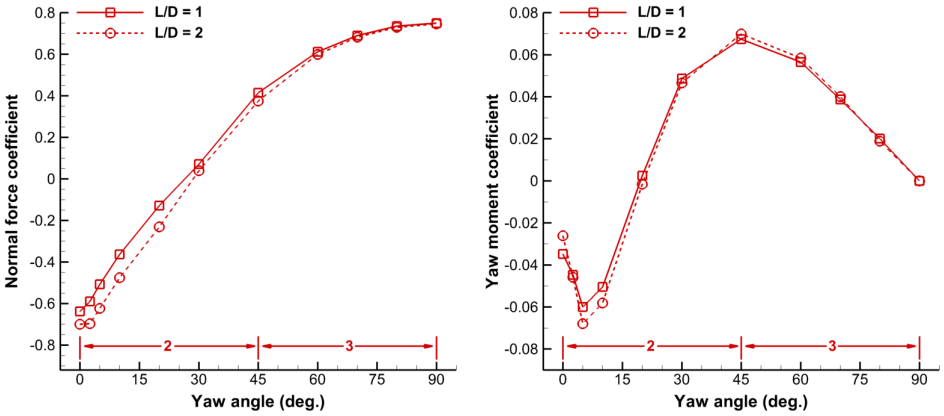

(a) Normal force coefficient (b) Yaw moment coefficient

Fig. 13: Normal force and yaw moment coefficients on flat faces with shear layer reattachment for the cylinder. The extents of the three shear layer behaviors from Fig. 7 are labeled.

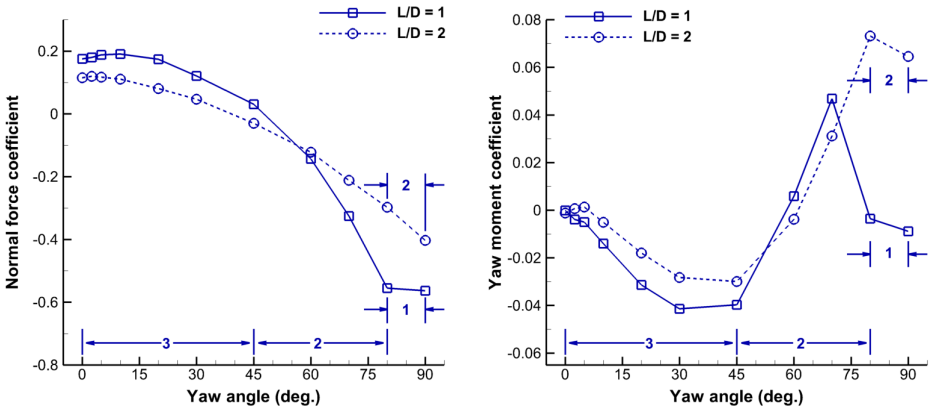

(a) Normal force coefficient (b) Yaw moment coefficient

Fig. 14: Normal force and yaw moment coefficients on curvilinear faces with shear layer reattachment for the cylinder. The extents of the three shear layer behaviors from Fig. 7 are labeled.

shedding frequency. This result is consistent with the experimental findings of Zdravkovich et al. [34], who observed significant variations in the Strouhal number of finite cylinders from one measurement to the next, particularly for L/D of two or less. The Strouhal numbers in Fig. 15 fall within the range of 0.15 – 0.3, which is in the same range observed by Zdravkovich and encompasses the 2-D cylinder "universal" value of 0.2. These results confirm that the concept of a universal Strouhal number is not as meaningful in the presence of highly 3-D flow, but the 2-D value of 0.2 is still typical for these 3-D aspect ratios.

4.6 Importance for Sling Loads

The quasi-steady aerodynamics of bluff bodies are very complex, and there are no rapid analytical theories that can be applied. However, the present work demonstrates that many aspects of the quasi-steady aerodynamics are common across bluff body types, in particular, the characteristic shear layer behavior on individual faces. The most significant differences arise from the fact that reattachment occurs at a different incidence angle for the different geometry types, but this angle can be predicted from the empirical curve fits of Fig. 11. Therefore, it is expected that empirical models of the trends presented in Figs. 12–14 may be developed, which can then be used to predict overall forces and moments on diverse bluff body types by summing the contributions from all faces, as developed and demonstrated by Greenwell[2] for 2-D rectangular bodies.

Prosser and Smith[17] have demonstrated that the unsteady aerodynamic effects arising from body motion may be modeled by a time-domain representation of classical theory. The model consists of a second-order differential equation with the quasi-steady aerodynamic coefficients forcing the system. This model is independent of geometry type, size, and flight speed. It may be applied to any dynamic bluff body, provided the quasi-steady coefficients are known, to introduce the theoretical unsteady aerodynamic phenomena.

Unsteady vortex shedding is also important for sling loads. The dashed bounding lines in Figs. 5 and 6 indicate that significant fluctuations exist in the forces and moments for bluff bodies. Prosser and Smith[17] have demonstrated that the fluctuating component of the aerodynamic coefficient can be written as the summation of a number of harmonic terms, and that a single harmonic term is adequate to model the fluctuations so long as the time-dependent term is a random function accurately representing the true turbulent shedding behavior. The shedding frequency is directly related to the Strouhal number. Figure 15 suggests that $St = 0.2$ is a reasonable estimate of the typical Strouhal number for 3-D bluff bodies which may be applied in reduced-order simulations.

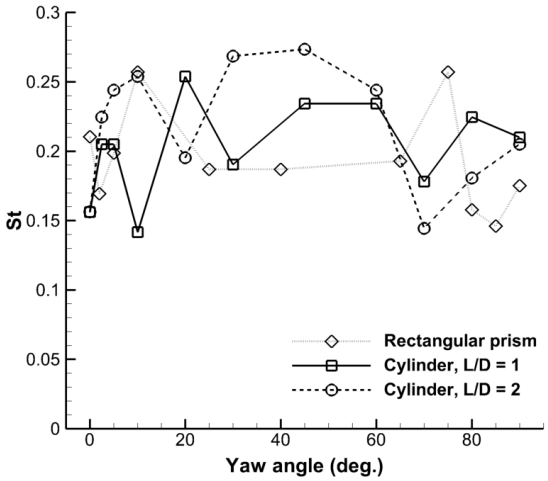

Fig. 15: Strouhal number variation with yaw angle.

The current work indicates that many aspects of the quasi-steady aerodynamics are similar for prisms and cylinders, so empirical models of these effects will form the foundation for a broadly-applicable model of the quasi-steady forces and moments. This approach promises significant advances in the prediction of sling load dynamics and stability with a minimum of computational, experimental, or flight testing expenses.

5 CONCLUSIONS

The three-dimensional aerodynamics of several canonical bluff bodies have been evaluated using computational-fluid-dynamics-based numerical experiments. The important findings include:

- The hybrid RANS-LES turbulence approach is able to accurately predict unsteady three-dimensional flows around rectangular prisms and finite cylinders.
- Sudden changes in the forces and moments are observed when the shear layer reattachment behavior changes, similar to those observed in 2-D rectangular experiments from the literature.
- Shear layer reattachment behavior is qualitatively similar for the rectangular prism and both finite cylinders studied, as well as that observed from the 2-D experiments in the literature.
- Reattachment angles for the 3-D rectangular prism fall on the same empirical curve fit from the literature on 2-D rectangular bluff bodies. Cylinder reattachment angles depend on the face type (flat or curvilinear), but not on the aspect ratios examined. The reattachment angle for a given normalized distance is less for a flat face than a curvilinear face, and both are less than that of the rectangular prisms.

- When the forces and moments are decomposed into contributions of individual faces, the effects of reattachment are readily apparent and very similar across the geometries studied. The similarities suggest that empirical models will be useful in developing broadly-applicable reduced-order models of the quasi-steady aerodynamics.
- The vortex shedding for 3-D bluff bodies is aperiodic, resulting in significant variations in the Strouhal number from one case to another. Strouhal numbers varied within the range 0.15 – 0.3 for the bluff bodies examined, consistent with the findings experimental findings from the literature.
- The trends and empirical models for quasi-steady and unsteady bluff body aerodynamics may be leveraged in reduced-order models for sling load dynamics and stability.

6 ACKNOWLEDGEMENTS

This research is funded through the U.S. Army/Navy/NASA Vertical Lift Rotorcraft Center of Excellence at Georgia Institute of Technology under Task 10 "Dynamic-Aerodynamic Interactions of Bluff Bodies: Computational Investigations" under the direction of Mahendra Bhagwat of AFDD, Agreement No. W911W6-11-2-0010. The authors would like to thank the technical points of contact of this project, Marty Moulton and Tom Thompson of AMRDEC for their insights, as well as noted researchers in sling loads: Luigi Cicolani, Doug Greenwell, and Aviv Rosen.

COPYRIGHT STATEMENT

REFERENCES

[1] Matheson, N., "The Stability of Portable Bridges Carried on Slings Beneath Helicopters," Technical Report 154, DSTO, UK, 1980.

[2] Greenwell, D., "Modelling of Static Aerodynamics of Helicopter Underslung Loads," *Aero. J.*, Vol. 115, (1166), April 2011, pp. 201–219.

[3] Raz, R., Rosen, A., Carmeli, A., Lusardi, J., Cicolani, L. S., and Robinson, L. D., "Wind Tunnel and Flight Evaluation of Stability and Passive Stabilization of Cargo Container Slung Load," 64th Am. Helicopter Soc. Annual Forum, April 29 – May 1, 2008.

[4] Shechter, E., "Bearing Heavy Loads," *Aerospace America*, June 2014, pp. 18–20.

[5] Cheng, M. and Liu, G., "Effects of Afterbody Shape on Flow around Prismatic Cylinders," *J. Wind Eng. and Ind. Aero.*, Vol. 84, (2), January 2000, pp. 181 – 196.

[6] Matsumoto, M., "Vortex Shedding of Bluff Bodies: A Review," *J. Fl. and Struct.*, Vol. 13, (7–8), October 1999, pp. 791–811.

[7] Matsumoto, M., Ishizaki, H., Matsuoka, C., Daito, Y., Ichikawa, Y., and Shimahara, A., "Aerodynamic Effects of the Angle of Attack on a Rectangular Prism," *J. Wind Eng. and Ind. Aero.*, Vol. 77–78, (7–8), September 1998, pp. 531–542.

[8] Modi, V. and Slater, J., "Unsteady Aerodynamics and Vortex Induced Aeroelastic Instability of a Structural Angle Section," *J. Wind Eng. and Ind. Aero.*, Vol. 11, (1–3), May 1983, pp. 321–334.

[9] Zaki, T., Sen, M., and Gad-el Hak, M., "Numerical and Experimental Investigation of Flow Past a Freely Rotatable Square Cylinder," *J. Fl. and Struct.*, Vol. 8, (7), 1994, pp. 555–582.

[10] Raz, R., Rosen, A., Carmeli, A., Lusardi, J., Cicolani, L. S., and Robinson, L. D., "Wind Tunnel and Flight Evaluation of Passive Stabilization of a Cargo Container Slung Load," *J. Am. Helicopter Soc.*, Vol. 55, (3), July 2010.

[11] Cicolani, L. S., Cone, A., Theron, J., Robinson, L. D., Lusardi, J., Tischler, M. B., Rosen, A., and Raz, R., "Flight Test and Simulation of a Cargo Container Slung Load in Forward Flight," *J. Am. Helicopter Society*, Vol. 54, (3), July 2009, pp. 1–18.

[12] Raz, R., Rosen, A., Cicolani, L. S., Lusardi, J., Gassaway, B., and Thompson, T., "Using Wind Tunnel Tests for Slung Loads Clearance," 67th Am. Helicopter Soc. Annual Forum, May 3–5, 2011.

[13] Prosser, D. T. and Smith, M. J., "Navier-Stokes-Based Dynamic Simulations of Sling Loads," Paper AIAA-2013-1922, AIAA Structures, Structural Dynamics, and Materials Conference, April 8–11 2013.

[14] Cicolani, L. and da Silva, G., J, "Unsteady Aerodynamic Model of a Cargo Container for Slung-Load," *Aero. J.*, Vol. 108, (1085), July 2004, pp. 357–368.

[15] Cone, A. C., *Simulation of a Cargo Container Slung Load at Speeds with Signficiant Aerodynamic Effects*, M.S., Cal. Polytechnic State University, 2007.

[16] Prosser, D. T. and Smith, M. J., "Characterization of Flow Around Rectangular Bluff Bodies at Angle of Attack," *Phys. Letters A*, Vol. 376, (45), 2012, pp. 3204 – 3207.

[17] Prosser, D. T. and Smith, M. J., "A Novel, High Fidelity 6-DoF Simulation Model for Tethered Load Dynamics," 70th Am. Helicopter Soc. Annual Forum, May 20 – 22 2014.

[18] Rosen, A., Cecutta, S., and Yaffe, R., "Wind Tunnel Tests of Cube and CONEX Models," Technical Report TAE 844, Technion – Institute of Technology, Faculty of Aerospace Engineering, November 1999.

[19] Cicolani, L., Lusardi, J., Greaves, L., Robinson, D., Rosen, A., and Raz, R., "Flight Test Results for the Motions and Aerodynamics of a Cargo Container and a Cylindrical Slung Load," Technical Report NASA/TP2010-216380, 2010.

[20] Lynch, C. E. and Smith, M. J., "Extension and Exploration of a Hybrid Turbulence Model on Unstructured Grids," *AIAA J.*, Vol. 49, (11), November 2011, pp. 2585–2590.

[21] Shenoy, R., Smith, M., and Park, M., "Unstructured Overset Mesh Adaptation with Turbulence Modeling for Unsteady Aerodynamic Interactions," *J. Aircraft*, Vol. 51, (1), January 2014.

[22] Anderson, W., Rausch, R., and Bonhaus, D., "Implicit/Multigrid Algorithms for Incompressible Turbulent Flows on Unstructured Grids," *J. Comp. Phys.*, Vol. 128, (2), 1996, pp. 391–408.

[23] Sánchez-Rocha, M. and Menon, S., "The Compressible Hybrid RANS/LES Formulation Using an Additive Operator," *J. Comp. Phys.*, Vol. 228, (6), April 2009, pp. 2037–2062.

[24] Smith, M. J., Liggett, N. D., and Koukol, B. C., "Aerodynamics of Airfoils at High and Reverse Angles of Attack," *J. Aircraft*, Vol. 48, (6), November–December 2011, pp. 2012–2023.

[25] Shenoy, R., Holmes, M., Smith, M. J., and Komerath, N., "Scaling Evaluations on the Drag of a Hub System," *J. Am. Helicopter Soc.*, Vol. 58, (3), July 2013, pp. 1–13.

[26] Noack, R., "SUGGAR: A General Capability for Moving Body Overset Grid Assembly," Paper AIAA-2005-5117, 17th Computational Fluid Dynamics Conference, June 2005.

[27] Noack, R., "DiRTlib: A Library to Add an Overset Capability to Your Flow Solver," Paper AIAA-2005-5116, 17th Computational Fluid Dynamics Conference, June 2005.

[28] Chorin, A., "A Numerical Method for Solving Incompressible Viscous Flow Problems," *J. Comp. Phys.*, Vol. 2, (1), 1967, pp. 12–26.

[29] Liggett, N. and Smith, M. J., "Temporal Convergence Criteria for Time-Accurate Viscous Simulations of Separated Flows," *Comp. & Fl.*, Vol. 66, 2012, pp. 140–156.

[30] Shenoy, R., *Overset Adaptive Strategies for Complex Rotating Systems*, Ph.D. thesis, Georgia Institute of Technology, Atlanta, Georgia, 2014.

[31] McCroskey, W., "The Phenomenon of Dynamic Stall," Technical Report NASA TM-81264, 1981.

[32] Mantri, R., Raghav, V., Komerath, N., and Smith, M. J., "Stability Prediction of Sling Load Dynamics Using Wind Tunnel Models," 67th Am. Helicopter Soc. Annual Forum, May 3–5, 2011.

[33] Hoerner, S., *Fluid-Dynamic Drag*, Hoerner Fluid Dynamics, Midland Park, NJ, 1958.

[34] Zdravkovich, M., Brand, V., Mathew, G., and Weston, A., "Flow Past Short Cylinders with Two Free Ends," *J. Fl. Mech.*, Vol. 203, June 1989, pp. 557–575.

[35] Robertson, J., Wedding, J., Peterka, J., and Cermak, J., "Wall Pressures of Separation – Reattachment Flow on a Square Prism in Uniform Flow," *J. Wind Eng. and Ind. Aero.*, Vol. 2, (4), January 1978, pp. 345–359.

[36] Norberg, C., "Flow around Rectangular Cylinders: Pressure Forces and Wake Frequencies," *J. Wind Eng. and Ind. Aero.*, Vol. 49, (1–3), December 1993, pp. 187–196.

[37] Da Matha Sant'Anna, F., Laneville, A., Trepanier, J., and Lu, Z., "Detailed Pressure Field Measurements for Some 2-D Rectangular Cylinders," *J. Wind Eng. and Ind. Aero.*, Vol. 28, (1–3), August 1988, pp. 241–250.

[38] Mulhearn, P., "Stagnation and Reattachment Lines on Cylinder of Square Cross-Section in Smooth and Turbulent Flows," *Nature Phys. Sci.*, Vol. 241, (113), February 1973, pp. 165–167.